CHEMISTRY OF MATERIALS

pubs.acs.org/cm

Article

Thermodynamic and Kinetic Barriers Limiting Solid-State Reactions Resolved through In Situ Synchrotron Studies of Lithium Halide Salts

Monty R. Cosby, Christopher J. Bartel, Adam A. Corrao, Andrey A. Yakovenko, Leighanne C. Gallington, Gerbrand Ceder, and Peter G. Khalifah*

Cite This: *Chem. Mater.* 2023, 35, 917−926

Read Online

ACCESS | Metrics & More | Article Recommendations | Supporting Information

ABSTRACT: Although halide salts such as LiCl and LiBr are routinely used as a source of Li ions during ion exchange reactions, a detailed understanding of the processes controlling the rates of these reactions is presently lacking. Recently, we discovered that the rate-limiting barriers for ion exchange are commonly associated with these salts rather than the ceramic target of ion exchange, making it important to quantitatively understand salt processes. Here, it is demonstrated that in situ synchrotron studies of ion exchange reactions can be used to precisely quantify the thermodynamic activation energies associated with these solid-state reactions in a manner that can be directly compared with predictions from density functional theory (DFT). While the temperature dependence of the LiCl reaction rate is found to be set by a barrier associated with ion hopping, it was discovered that for LiBr, the rate is also affected by the defect formation energy—an energy found to be substantially lower than predicted by DFT. Furthermore, it is shown that by varying the relative amounts of reactants, the resulting change in reaction rate can be used to identify the rate-limiting reagent and to elucidate an overall scaling relationship that controls the concentration dependence of the reaction rate. Also, it is demonstrated that global fits across doped and undoped salts can be used to probe both intrinsic and extrinsic vacancy concentrations. This improved understanding of ion exchange mechanisms can be used to predict reaction conditions that can accelerate ion exchange reaction rates by orders of magnitude. The techniques demonstrated here can be broadly applied to probe the kinetics and thermodynamics of solid-state reactions.

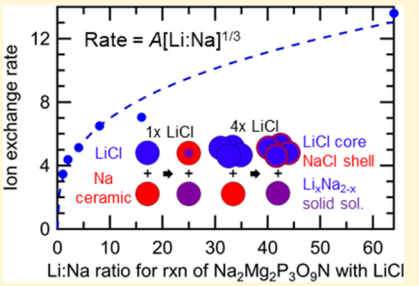

INTRODUCTION

It has long been recognized that ion exchange reactions provide an important pathway for accessing metastable materials that cannot be prepared through direct solid-state synthesis. This has been commonly exploited for fundamental purposes such as materials discovery, for example, using topotactic transformations that provide control over the target structure.[1,2] Ion exchange is also frequently used for applied purposes, such as transforming a Na-ion electrode material or solid-state electrolyte into its Li-ion equivalent.[3−6]

Despite the importance of ion exchange reactions, relatively little is known about the variables that control the rates of ion exchange due to the challenges involved in precisely measuring ion exchange kinetics. We have recently demonstrated that in situ synchrotron X-ray diffraction (XRD) experiments are a powerful and efficient tool for following solid-state ion exchange reaction kinetics,[7] and that the reaction progress generally has a $t^{1/2}$ time dependence indicative of random walk diffusional processes.[8,9] Our efforts were focused on the ion exchange synthesis of CUBICON-type $Li_2Mg_2P_3O_9N$, both due to its potential utility as a solid-state electrolyte[3] and to our existing understanding of CUBICON ion hopping pathways[10] and phase transformation mechanisms.[3] Surprisingly, our initial studies found that the rate for the solid-state Li-ion exchange reaction $Na_2Mg_2P_3O_9N + nLiX \rightarrow Na_{2-x}Li_xMg_2P_3O_9N + nLi_{(1-x/n)}Na_{x/n}X$ was different for every different halide (X) salt studied, indicating that transport processes in the salt and not the ceramic are rate-limiting.[7] This indicates that to understand and control the overall ion exchange reaction, it is necessary to have a detailed mechanistic understanding of the ion exchange processes that occur within the salt.

In the present work, a deeper understanding of transport processes in halide salts has been pursued in two ways. First, the thermodynamic activation energies, E_a, that limit ion exchange were characterized through a combination of temperature-dependent experiments and density functional theory (DFT) calculations. This enables both the quantifica-

Received: August 18, 2022
Revised: December 22, 2022
Published: January 20, 2023

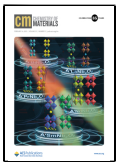

tion of activation energies and, in many cases, their atomic origin to be resolved. Second, the dependence of the reaction rate on the relative amounts of the two reactants (salt and ceramics) was investigated since these effects are substantial. From these results, a universal scaling relationship was observed that enables prediction of reaction rates. This scaling relationship is expected to be generally applicable to solid-state reactions. Finally, it was demonstrated that it is possible to characterize vacancy concentrations through multisample fitting. In all cases, these novel insights were enabled by infrastructure advances for rapidly collecting and analyzing synchrotron XRD data.

EXPERIMENTAL SECTION

$Na_2Mg_2P_3O_9N$ was synthesized by combining stoichiometric amounts of $MgCO_3$ (J. T. Baker, 99%), $(NH_4)_2HPO_4$ (AMRESCO, >90%), and $[Na(PO_3)]_n$ (Sigma, $n = 6$) and then grinding by hand in an agate mortar and pestle for 15 min. The resulting mixture was transferred to a boat made from Mo foil (99.95%, 0.05 mm thick, Fischer Scientific) and loaded in a tube furnace (Lindberg/BlueM Mini-Mite). The synthesis was performed under NH_3 gas (30−40 mL/min) with the sample heated to 780 °C (200 °C/h ramp rate), held for 20 h, and cooled (200 °C/h) to room temperature, after which the furnace was purged with N_2 gas. The purity of the powder product was confirmed by powder XRD (Bruker D8 Advance with a Cu K_α source, variable slits, and a LynxEye detector). The anhydrous salts LiCl (Sigma-Aldrich, >99.98%) and LiBr (Alfa Aesar >99.995%) were used as received and were handled in a glovebox to avoid hydration. Mg-substituted salts were prepared by dissolving a Li halide salt with either $MgCl_2$ (Fischer Scientific, 99.99%) or $MgBr_2$ (Sigma-Aldrich, >99.99%) in water and then evaporating to dryness under vacuum at room temperature in a vacuum oven. Although nominally doped at the 1% level, the actual Li:Mg molar ratio based on weights was 95.58:1.00 for $Li_{1-2x}Mg_xCl$ (corresponding to $x = 0.01025$) and 98.82:1.00 for $Li_{1-2x}Mg_xBr$ ($x = 0.009918$), with the single-phase nature of substituted products confirmed by power XRD.

For in situ synchrotron diffraction studies of ion exchange, either the pure or nominally 1% Mg-substituted salts were ground together with $Na_2Mg_2P_3O_9N$ within an Ar-filled glovebox. The mixtures were then loaded in glass NMR tubes (3 mm diameter, Wilmad Type 1, Sigma-Aldrich), sealed with epoxy (Loctite E-30CL, 30 min set time), and flame-sealed outside of the glovebox with a small hand-held butane torch. The Li:Mg molar ratios of the nominally 1% substituted salts are reported in Table S1 and the actual Na:Li molar ratios for each sample are in Table S2.

In situ diffraction studies were performed remotely at beamlines 17-BM and 11-ID-B at the Advanced Photon Source each using an amorphous silicon-based area detector (PerkinElmer). Experiments utilized a stainless steel eight-well NMR tube furnace that we described previously.[7] The furnace was heated to desired temperatures at a fast ramp rate of 100 °C/min, allowing the final temperature to be reached in about 5 min, although an additional ∼5 min was often needed for the temperature to fully stabilize. Reactions at 11-ID-B were carried out at a distance of 1000 mm with an energy of 58.6 keV ($\lambda = 0.2115$ Å, 2 s total exposure time). At 17-BM, ion exchange was performed at a distance of 1000 mm with an energy of 51.4 keV ($\lambda = 0.24098$ Å, 2 s total exposure time). Scans for each sample were taken approximately once every 50 s at 11-ID-B and every 70 s at 17-BM.

The resulting diffraction data were integrated with a python code utilizing the pyFAI software package.[11] Detector parameters (distance and tilts) and instrumental contributions to peak shape were empirically determined using data from a Si SRM640f calibrant. A representative Rietveld refinement control file for TOPAS[12] (Bruker AXS, v6) is provided in the Supporting Information. Plotting and fitting of lattice parameters to kinetic models were done in Igor Pro, v8.

DFT calculations were performed using the Vienna Ab Initio Simulation Package.[13] The generalized gradient approximation as formulated by Perdew, Burke, and Ernzerhof[14] and the projector augmented-wave method[15] were used with an energy cutoff of 520 eV. Initial cubic unit cell structures of LiCl, NaCl, LiBr, and NaBr were extracted from the Materials Project database.[16] Expanded 3 × 3 × 3 supercells were generated and their geometries were optimized with 2 × 2 × 2 Monkhorst−Pack[17] k-point grids generated using pymatgen.[18] Energies were converged to 10^{-5} eV for electronic relaxations and 0.005 eV/Å for ionic relaxations. Nudged elastic band (NEB) calculations were performed for Li^+ and Na^+ vacancy-mediated hopping in the dilute vacancy limit using the climbing image approach[19] with each image converged to 10^{-4} eV for electronic relaxations and 0.05 eV/Å for ionic relaxations. A uniform background charge was used to compensate for the cation vacancies.

RESULTS AND DISCUSSION

In order to gain a deeper understanding of the transport processes in halide salts that commonly limit the overall rate of solid-state ion exchange, studies were carried out for the salt-limited synthesis reactions of $Li_2Mg_2P_3O_9N$: $Na_2Mg_2P_3O_9N + n\mathrm{LiX} \rightarrow Na_{2-x}Li_xMg_2P_3O_9N + n\mathrm{Li}_{(1-x/n)}\mathrm{Na}_{x/n}\mathrm{X}$. Although we previously investigated the baseline kinetics for a variety of halide salts (X = F, Cl, Br),[7] the complementary thermodynamic activation energies that provide the best insights into the reaction mechanism have not yet been resolved and thus motivate the present work. Due to the slow reaction rates when LiF is used as the salt source, these efforts focused on the salts LiCl and LiBr and their Mg^{2+}-substituted variants ($Li_{1-2x}Mg_xX$) with engineered vacancies that are known to have higher ionic conductivities.[20]

Extraction of Kinetic Data. The ion exchange of Li into $Na_2Mg_2P_3O_9N$ ($a = 9.2439$ Å) is known to proceed through a three-stage process beginning with two distinct solid solutions and finishing with a two-phase reaction to form $Li_2Mg_2P_3O_9N$ ($a = 9.1118$ Å).[3] For the present work, kinetic data were analyzed exclusively for the early stages of this reaction (in which it proceeds through two solid solutions) under the assumption that the lattice parameter rates of change during the two successive solid solutions are indistinguishable. For each time point, the reaction progress was characterized by diffraction data using the framework that we recently developed.[7] Specifically, it was assumed that reaction progress is proportional to the change in the cubic a-lattice parameter—an assumption that (like Vegard's law) is not strictly true but which holds within the precision of the present data since the changes in unit cell volume (which should change linearly with the degree of substitution) are very small (<0.2%) in the regions being used for kinetic analysis during ion exchange. A representative Rietveld refinement of a single diffraction pattern is shown in Figure S1, and the rate constants obtained for all samples are given in Table S3.

A representative set of reaction data for four salts (LiCl, LiCl: 1% Mg and LiBr, LiBr: 1% Mg) studied at 375 °C are shown in Figure 1. It can be clearly seen that ion exchange proceeds more slowly for LiCl than for LiBr, consistent with the previously established reaction rate trends of LiF < LiCl < LiBr. Even though Mg substitution was done only at the 1% level, the effect on the reaction rate was large. The reaction progress for both substituted samples was nearly double that of their unsubstituted analogs after 4 h of reaction.

For all samples, it is seen that the cubic a-lattice parameter evolves after temperature stabilization (∼4 min) as

https://doi.org/10.1021/acs.chemmater.2c02543
Chem. Mater. 2023, 35, 917−926

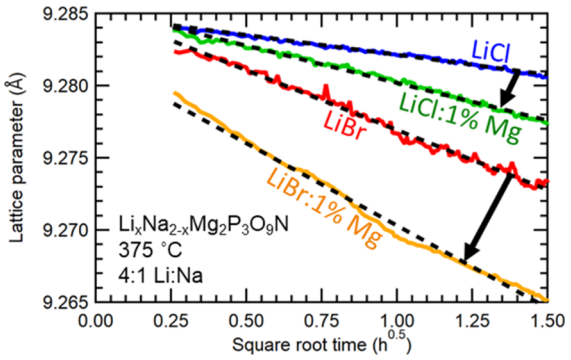

Figure 1. Evolution of lattice parameters during Li-ion exchange of $Na_2Mg_2P_3O_9N$ at 375 °C with a 4:1 Li:Na molar ratio. Black dashed lines indicate the fits used to determine the lattice-based rate constant, $k_{lattice}$. Data prior to temperature stabilization (~4 min) are omitted. Each 0.001 Å change in the lattice parameter corresponds to the reaction proceeding by about 0.75%, so the ion exchange reaction is about 10% complete for the maximally reacted sample (LiBr: 1% Mg).

$$a = a_0 + kt^{1/2} \quad (1)$$

From the linear region of the data, we, therefore, extract a rate parameter $k_{lattice}$ which we report in units of Å/$h^{1/2}$. This behavior indicates that the overall reaction rate is not simply proportional to the ionic conductivity, σ_i, which is expected to remain constant throughout the analyzed stages of the reaction. It instead reflects the fact that in the absence of a bias pushing the ions in the same direction (as would be the case if the ionic conductivity was measured in a circuit), the reaction front proceeds with the $t^{1/2}$ dependence characteristic of random walk behavior even when σ_i is time independent. However, it is expected that the rate constant k is proportional to σ_i.

Determination of Activation Energies. The overall activation energy, E_a, associated with ion exchange for a given salt source was determined experimentally by carrying out kinetic studies at five different temperatures (typically from 325 to 425 °C). A representative set of data for LiCl are shown in Figure 2. The thermal expansion causes the initial lattice parameters at t = 0 to differ for data collected at different temperatures, with these changes being comparable in magnitude to the lattice parameter changes that occur due to ion exchange. In all cases, consistent $t^{1/2}$ behavior was observed for a sufficiently long period to enable reaction rates (k) to be precisely determined despite the very small changes in the lattice parameter (<0.02 Å). Even though the data were collected at two beamlines across multiple experiments, comparisons of common samples indicated good reproducibility (Figure S3).

When the overall activation energies for ion exchange using LiCl and LiBr are estimated through Arrhenius-type plots and fits (Figure 3), large differences are observed. The activation energy of 1.21(2) eV determined for LiBr is about double the 0.62(3) eV activation energy for LiCl. Curiously, ion exchange reactions generally proceeded more quickly for LiBr than for LiCl despite the much higher energy barrier. This behavior suggests that different processes are limiting ion exchange for these two closely related salts.

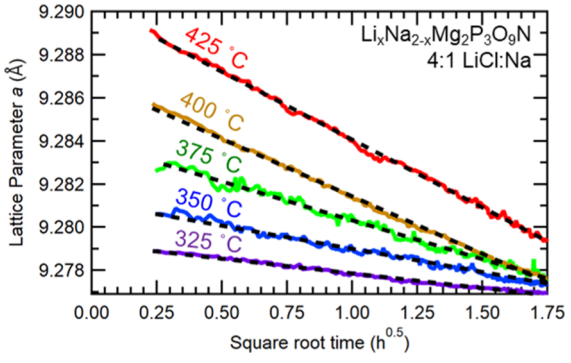

Figure 2. Temperature-dependent evolution of lattice parameters during Li-ion exchange of $Na_2Mg_2P_3O_9N$ done at a 4:1 Li:Na ratio. Black dashed lines indicate the fits used to determine the lattice-based rate constant, $k_{lattice}$.

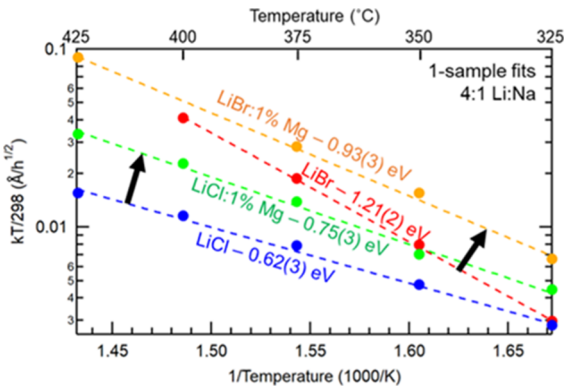

Figure 3. Rate data for $Na_2Mg_2P_3O_9N$ ion exchanged with LiCl and LiBr (both undoped and doped with 1% Mg) on an Arrhenius-type plot. Lines indicate independent fits to a single overall E_a for each salt composition with fit values labeled on the plot. Fits were to the one-sample equation of $kT \propto \exp(-E_a/kT)$. As indicated by the axis label, kT values have been divided by 298 K so values will be close to the values of the rate constant.

One possible origin for the different behavior may be substantially different barriers for ion hopping in the halide and bromide lattices. It is not known a priori whether the rate-limiting barrier is associated with the motion of the Li^+ ions leaving the salt or the motion of the Na^+ ions entering the salt. The consistent rate behavior seen throughout the ion exchange process (Figure 2) suggests that the height of the limiting barrier does not substantially change as the salt composition evolves across the $Li_{1-x}Na_xCl$ or $Li_{1-x}Na_xBr$ solid solutions during ion exchange reactions.

DFT calculations using the NEB method have previously been demonstrated to be effective in calculating transition state energies associated with ion motion, with especially good correlations between theoretical predictions and experimental results seen for closed-shell compounds.[21,22] These methods were used to calculate the energy for Li^+ ions in LiX salts and Na^+ ions in NaX salts (X = Cl, Br) to hop into a pre-existing vacancy. The energy along the NEB trajectory is plotted in Figure 4 and the hopping activation energies, E_{hop}, are provided in Table 1. In all cases, the barrier for Na^+ is about 0.2 eV higher than for Li^+, with a maximum value of 0.59 eV for X = Cl and 0.55 eV for X = Br. These calculated E_h energies are in good agreement with the activation energies for ion conduction previously measured using alternating current electrochemical impedance spectroscopy (EIS) methods[23−26] (Table 1), suggesting that the single-ion hopping mechanism is appropriate.

https://doi.org/10.1021/acs.chemmater.2c02543
Chem. Mater. 2023, 35, 917−926

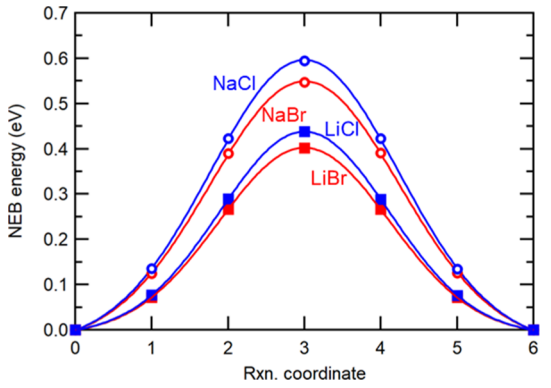

Figure 4. Energetics of ion hopping in halide salts calculated through DFT using NEB methods. The energies for Li^+ motion (solid squares) and Na^+ motion (open circles) within a chloride matrix (blue) or a bromide matrix (red) are shown. Gaussian fits are overlaid with extracted E_a values provided in Table 1.

Table 1. DFT-Calculated and Literature-Measured (EIS) Activation Energies, E_{hop}, for Ion Hopping in Halide Salts

Salt	$E_{hop,DFT}$	E_{hop},E_{IS}	$E_{Schottky,EIS}$	$E_{Schottky,DFT}$
LiCl	0.437	0.41[23]	2.12[23]	1.73[24]
LiBr	0.402	0.39[23]	1.80[23]	1.54[24]
NaCl	0.594	0.67[24]	2.30[26]	2.32[24]
NaBr	0.547	0.64[24]	1.72[25]	2.13[24]

Based on the DFT-calculated and literature E_{hop} values, it can be concluded that the E_a for ion exchange using LiCl determined experimentally in this work reflects an ion hopping energy. Additionally, it is likely that E_a derives from the barrier for Na^+ motion rather than Li^+ motion. However, the much larger measured E_a for LiBr must have a different origin. Based on the response the E_a for these two salts has when Mg is doped to introduce 1% of vacancies (Figure 3), it can be concluded that E_a for LiBr additionally reflects the contribution of a vacancy formation energy E_{vac} for reasons discussed in more detail below.

Under conditions where the overall rate of ion exchange is limited by a single species in a single phase, the rate constant k for ion exchange should be proportional (through a prefactor we denote A) to the product of the number of available sites to hop from, the number of available sites to hop to, and the probability of a hop being successful.[27,28] If we assume that the number of sites to hop from remains constant—an assumption justified by the successful fitting of our data—then this relationship becomes

$$kT = A[V_{imp} + V_{dop} + \exp(-E_{vac}/kT)] \times \exp(-E_{hop}/kT) \quad (2)$$

Here, the first part of the expression after the prefactor describes the vacancy concentration as the sum of two extrinsic terms, one from impurities (V_{imp}) and one term from intentional doping (V_{dop}), and one intrinsic term with formation energy denoted E_{vac}.

E_{vac} represents the formation energy of a single vacancy, and as such is the general quantity that will be directly extracted from fits to experimental data in the absence of knowledge of a specific defect formation model. Early DFT calculations predicted Schottky defects (paired cation and anion defects) to be the lowest energy defects in the salts studied in this work.[23,24] Schottky defect formation energies, $E_{Schottky}$, from those studies are given in Table 1 alongside values inferred from early EIS studies.[23−26] When vacancy calculations are done directly with the energy of the Schottky pair (as is traditionally the case), the equivalent exponential term is $\exp(-E_{Schottky}/2kT)$. As such, the mathematical relationship $E_{vac} = E_{Schottky}/2$ is necessarily true even though the energy of the cation and anion vacancies cannot be separately resolved. In our data fitting, we work with the general term of E_{vac} rather than specific quantity of $E_{Schottky}$ so that analysis results will be independent of the defect type.

This rate expression will exhibit two different types of exponential behavior depending on the relative amounts of extrinsic (V_{ext}) and intrinsic (V_{int}) defects, behavior that has previously been experimentally observed for other electronic and ionic conductors.[23−26] In either of these limits, the logarithm of kT should vary linearly when plotted against $1/T$ (as was done for Figure 3) while the intermediate regime between these limits should result in weakly nonlinear behavior. This cross-over behavior is illustrated for simulated data in Figure 5. In the extrinsic limit of $V_{ext} \gg V_{int}$, the overall

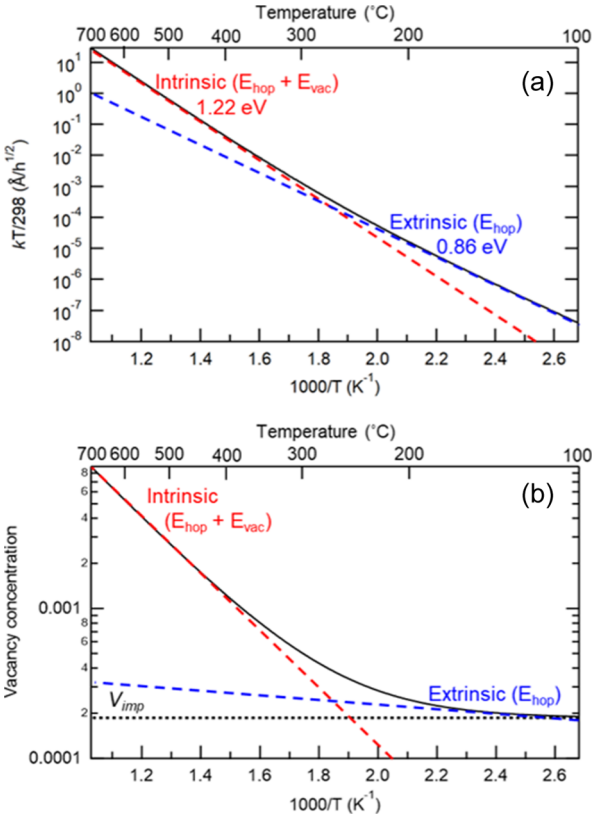

Figure 5. Simulated temperature-dependent (a) rate constants and (b) vacancy concentrations for LiBr using eq 2 showing the crossover from extrinsic ($E_a \propto E_{hop}$) to intrinsic ($E_a \propto E_{hop} + E_{vac}$) transport based on the fit parameters discussed in the next section.

activation energy will reduce to $E_a = E_{hop}$, as appears to be the case for LiCl both before and after doping. However, in the intrinsic limit of $V_{int} \gg V_{ext}$, then $E_a \approx (E_{hop} + E_{vac})$ through the product rule for exponents, leading to a very different observed E_a for the process even if the hopping mechanism does not change—exactly the difference in the type of behavior observed when comparing undoped LiBr to Mg-doped LiBr.

Using this framework, it is possible to understand the different behaviors of these four samples. All four samples

https://doi.org/10.1021/acs.chemmater.2c02543
Chem. Mater. 2023, 35, 917−926

exhibit linearity, as shown in Figure 3, and thus are likely to be in either the extrinsic or intrinsic limit under experimental conditions. When fit independently, both doped and undoped LiCl have similar activation energies that are comparable to DFT predictions. It is virtually certain that 1% Mg-doped LiCl is more robustly in the extrinsic regime than undoped LiCl, so the slightly higher (by 0.13 eV) E_a inferred for Mg-doped LiCl in the fits of Figure 3 should reflect the dopant slightly increasing the rate-limiting hopping barrier, E_{hop}, as might be expected for the stronger attraction between the cation vacancy and the divalent dopant. If this is indeed the origin, it should be expected that E_{hop} will continuously vary with the dopant concentration rather than being single valued and thus may need to be reinvestigated if reactions with salts at different Mg-doping levels are the focus of future studies.

Estimation of Vacancy Concentrations. One advantage of studying a family of related compounds instead of studying compounds individually is that more information than just an overall E_a can be extracted when global fitting methods are used. For example, the impurity vacancy concentration V_{imp} cannot be deconvoluted from prefactor A when fitting the LiCl data alone. Similarly, in the fitting of Mg-doped LiCl, V_{imp} is too small to resolve against the much larger doped vacancy concentration, V_{dop}. However, a two-sample global fit against the two sets of chloride experiments in which A and V_{imp} are assumed and constrained to be equal for the two samples allows V_{imp} to be determined with the quality of the fit to the data being comparable to the independent fits to the two data sets (Figure 6a). The full set of fit parameters is reported in Table 2. The fraction of impurity-derived vacancies estimated in this manner is 0.0047, a number that is small but which far exceeds the fraction of intrinsic vacancies ($\sim 10^{-8}$) that would be present at reaction temperatures based on DFT-calculated values of $E_{Schottky}$ reported in Table 1. As such, it should be concluded that the energy for forming intrinsic defects in LiCl is sufficiently high that they comprise a negligible fraction of the total number of vacancies in the sample, making it impossible to experimentally determine the vacancy formation energy E_{vac} for LiCl using the present experimental data.

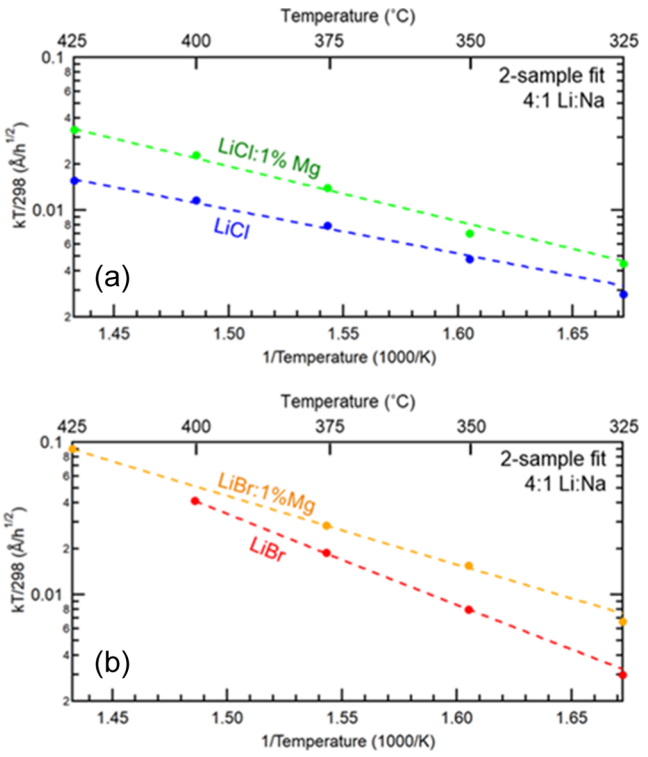

Figure 6. Rate data for $Na_2Mg_2P_3O_9N$ ion exchanged with LiCl and LiBr (both undoped and doped with 1% Mg) on an Arrhenius-type plot. Dashed lines indicate constrained fits to a combined two-sample fit with fit parameters given in Table 2.

Table 2. Parameters from One-Sample and Two-Sample Fits[a]

Salt	Parameter	One-sample		Two-sample
LiCl	E_a/E_{hop}	**0.62(3)**	/	**0.58(5)**
LiCl:Mg	E_a/E_{hop}	**0.75(3)**	/	**0.72(3)**
LiBr	E_a/E_{hop}	**1.21(2)**	/	*0.86*(4)
LiBr:Mg	E_a/E_{hop}	**0.93(3)**	/	*0.86*(4)
LiCl	E_{vac}	N/A		Large
LiCl:Mg	E_{vac}	N/A		Large
LiBr	E_{vac}	N/A		*0.40*(8)
LiBr:Mg	E_{vac}	N/A		*0.40*(8)
LiCl	V_{imp}	N/A		*0.005*(5)
LiCl:Mg	V_{imp}	N/A		*0.005*(5)
LiBr	V_{imp}	N/A		$2(2) \times 10^{-4}$
LiBr:Mg	V_{imp}	N/A		$2(2) \times 10^{-4}$
LiCl	A	N/A		$4(2) \times 10^{5}$
LiCl:Mg	A	N/A		$4(2) \times 10^{5}$
LiBr	A	N/A		$\mathbf{1(1) \times 10^{8}}$
LiBr:Mg	A	N/A		$\mathbf{1(1) \times 10^{7}}$

[a]Parameters freely refined are shown in bold, constrained shown in italics, and fixed shown without emphasis. V_{dop} was fixed at 0.01025 (LiCl:Mg), 0.009918 (LiBr:Mg), or 0. "Large" indicates values beyond the sensitivity limits of the refinement.

Analogous two-sample fits to the two bromide salts were also done (Figure 6b), although the results are both fundamentally different and more challenging to interpret. In contrast to the chloride system, Mg doping resulted in a decrease in the overall E_a for ion exchange, suggesting that intrinsic vacancies are the dominant type of vacancies in undoped LiBr. Based on eq 2, it is expected that $E_a \sim E_{hop} + E_{vac}$, which is generally observed when fitting the data. However, the addition of E_{vac} as a fit parameter results in severe correlations during fitting with the uncertainty of this parameter often exceeding its value—perhaps not surprisingly since only two salt compositions were used for fitting. Over a wide range of tested constraints and parameter values, it was typically found that $0.35 < E_{vac} < 0.40$ and $0.7 < E_{hop} < 0.9$. When refined independently, the E_{hop} values for doped and undoped LiBr typically differed by less than 0.1 eV, with the larger value sometimes belonging to the doped sample and sometimes belonging to the undoped sample.

The correlations also strongly affected the refinement of V_{imp}, which robustly refined to values lower than found for LiCl, and even refined to negative values under certain choices of constraints. In particular, it was found that constraining the prefactor A to be equal for doped and undoped LiBr commonly led to negative values of V_{imp} (though the total vacancy concentration always remained positive). While there are situations where a negative V_{imp} is plausible (e.g., a class of impurities that can compensate and neutralize vacancies), it was judged more likely that this is a fitting artifact. When the A values for the undoped and doped samples were refined independently, the former was typically 5−15× larger than the

https://doi.org/10.1021/acs.chemmater.2c02543
Chem. Mater. 2023, 35, 917−926

latter, suggesting that different values should be used for the two samples. The expectation of equal prefactors is predicated on the expectation of equal particle sizes. Given the substantially different preparation methods for the undoped sample (ground powder from the bottle) and the doped sample (salts were dissolved, precipitated, and then dried), it is very possible that these two specific samples have different particle sizes and thus should not be fit using common A values.

The final fitting of the two bromide samples was carried out with V_{imp} and E_{hop} constrained to be equal and V_{dop} constrained to the value calculated based on the sample stoichiometry, and all other parameters were freely refined with the values for all parameters given in Table 2. Although there are very large statistical uncertainties in many parameters, the parameter values demonstrated enough consistency across many trial refinements to be worth reporting. The vacancy concentration from impurities refined to a value of V_{imp} = 0.0002 is similar in magnitude but slightly smaller than that refined for LiCl. The constrained refinement value of E_{hop} (0.86 eV) for the bromide samples is modestly higher than values from EIS experiments for NaBr (0.64 eV) and DFT calculations for LiBr (0.55 eV), and these values should be considered to be in agreement within the fitting uncertainties. In contrast, the refined E_{vac} ($=E_{Schottky}/2$) value of 0.40 eV is about a third of what is expected based on both the present and past DFT calculations. If E_{hop} was overestimated in fitting and is instead assumed to have the EIS value of 0.65 eV, the value of E_{hop} would only rise to about 0.55 eV and would still only be about half of the expected value for Schottky defects. This strongly suggests that there may be a previously unrecognized low-energy defect formation mechanism for LiBr that has a dominant effect on its mobility and that further investigations to understand this defect are merited.

Our analysis of the presently available data shows that multisample fitting to determine vacancy concentrations in future studies can be made more robust in two ways that mitigate the limitations inherent to the present data. First, by examining a larger range of doping levels, it should be possible to significantly reduce the uncertainty in V_{imp} and to accurately determine extrinsic vacancy concentrations even when the amounts are small. Second, doing syntheses in a manner that leads to common particle sizes for all samples will minimize variations in the A prefactors. This should enable more robust parameter determination in a single class of samples (e.g., bromides) as well as to potentially even allow for global fitting that spans different classes of halides (e.g., combined fitting of chlorides and bromides).

Concentration Effects and Identification of Rate-Limiting Reactant. In our prior proof-of-principle in situ synchrotron diffraction experiments studying ion exchange kinetics, it was observed that the reaction rate had an unexpectedly strong dependence on the relative amounts of the ceramic ($Na_2Mg_2P_3O_9N$) and halide salt (LiX) precursors.[7] However, the detailed nature of this relationship could not be resolved due to the limited number of concentrations tested and the absence of temperature-dependent data. In the present work, we have studied a far more comprehensive set of samples that span five different temperatures and span reactant ratios varying from 1:1 to 64:1, where the ratio denotes the molar ratio of Li ions in the LiCl salt to Na ions in the $Na_2Mg_2P_3O_9N$ ceramic. The rate constants for each of these reactions with LiCl are plotted together in Figure 7.

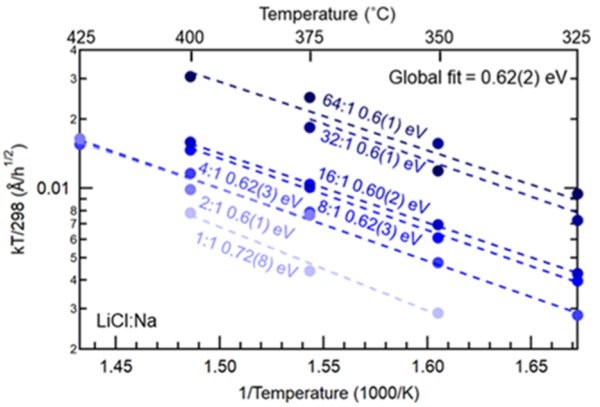

Figure 7. Concentration dependence of reaction rates (k) and activation energies (E_a, fits shown as dashed lines) for ion exchange of $Na_2Mg_2P_3O_9N$ with LiCl.

The very close agreement between the activation energies (~0.62 eV) obtained from Arrhenius-type fits to the data at each of the seven different studied concentrations in Figure 7 indicates that the reaction mechanism is similar in all cases despite the extent of the ion exchange differing by nearly an order of magnitude across the different reaction conditions. This suggests that the observed concentration dependence of reaction rates has a common physical origin. This was explored further by plotting the dependence of the reaction rate on the Li:Na ratio on a log−log plot, with data for each temperature shown in a different color (Figure 8a). The linearity of these data suggests a simple power law dependence of the reaction rate on the Li:Na molar ratio, R, with global fits of the rate data at all temperatures to $k = k_0 \cdot R^n$ finding a best-fit power of n = 0.37(3) when using a different prefactor k_0 for each temperature.

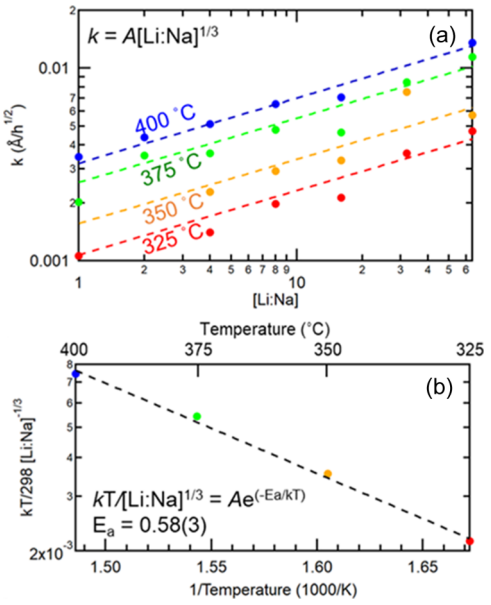

Figure 8. (a) Dependence of LiCl reaction rate on the Li:Na molar ratio, R, shown on a log−log plot with power law fits to $k = k_0 R^{1/3}$ shown as dashed lines. (b) Determination of overall activation energy from normalized reaction rates obtained through power law fits for each temperature, with the dashed line showing the best fit to the equation $kT/(R^{1/3}) = A \exp(-E_a/kT)$.

https://doi.org/10.1021/acs.chemmater.2c02543
Chem. Mater. 2023, 35, 917−926

The best-fit power is near the rational ratio of 1/3, so the suitability of this ideal ratio was tested in global fits. The use of $n = 1/3$ did not substantially change the quality of the fit (χ^2 increased by 20% from 1.24×10^{-5} to 1.45×10^{-5}). Furthermore, a plot of the k_0 values obtained using $n = 1/3$ showed clear Arrhenius behavior (Figure 8b) governed by an activation energy of $E_a = 0.58(3)$ eV that is in close agreement with values obtained independently for different Li:Na ratios. As such, this behavior appears to be representative of a fundamental relationship that governs reaction rates that can be used in a predictive manner.

Furthermore, the dependence of reaction rate on the Li:Na ratio allows the limiting reagent to be clearly identified as LiCl rather than $Na_2Mg_2P_3O_9N$. The reaction rate decreases monotonically as the relative amount of LiCl decreases and this trend extrapolates to a zero-reaction rate when no LiCl is present (Figure 9a). When the inverse ratio (Na:Li instead of Li:Na) is plotted in a similar manner (Figure 9b), the data can still be fit to a simple scaling relationship. However, the reaction rate increases as the Na:Li ratio decreases and additionally extrapolates to infinity as the relative amount of $Na_2Mg_2P_3O_9N$ goes to zero. As such, it is clear that $Na_2Mg_2P_3O_9N$ is not limiting the reaction rate.

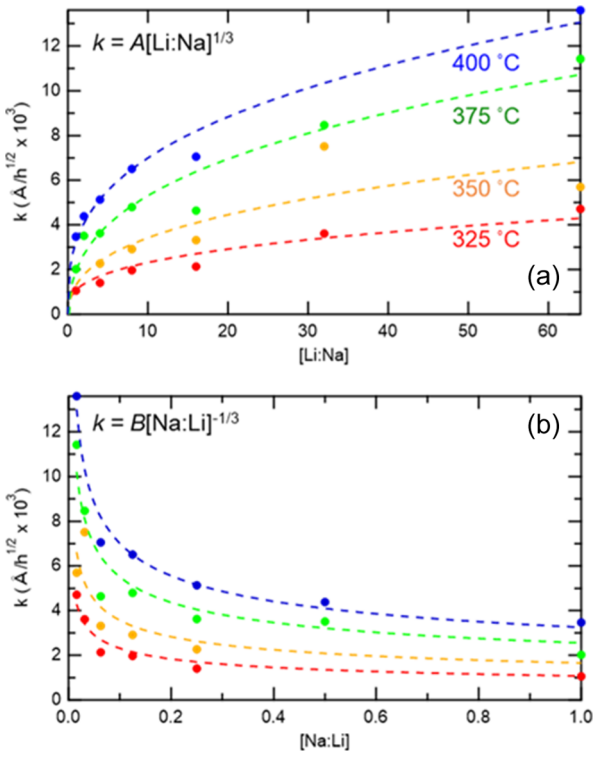

Figure 9. LiCl reaction rate plotted as a function of (a) Li:Na molar ratio and (b) Na:Li molar ratio, with fits to reaction rates measured at each temperature to a power law indicated with a dashed line. Only the plot against the Li:Na ratio extrapolates to a rate of zero at zero concentration, indicating that the overall rate is limited by the Li-containing species (LiCl) rather than the Na-containing species ($Na_2Mg_2P_3O_9N$).

While the limiting role of salt in these particular ion exchange reactions was already known from our variational studies comparing the relative reaction rates when different salts were used as a reactant (LiF, LiCl, and LiBr),[7] analogous studies cannot be done for generic solid-state reactions that are not ion exchange reactions. For example, in the synthesis of $CaO + TiO_2 \rightarrow CaTiO_3$, neither precursor can be substituted without changing the reaction product and/or the reaction mechanism. However, following changes in the reaction rate as the CaO/TiO_2 molar ratio is varied will allow the limiting reagent in this solid-state reaction to be identified without changing reaction precursors.

Although the cube root dependence of the reaction rate on the Li:Na ratio is robustly observed over a wide range of concentrations and temperatures corresponding to many different extents of reaction, the origin of this behavior is not yet clear. The rational fraction of 1/3 does hint at a geometric origin, especially since the overall activation energy E_a does not change over the studied reaction conditions. Since it has been clearly established that the amount of LiCl is limiting the reaction rate and that the overall reaction rate has a $t^{1/2}$ dependence indicative of a process limited by random walk diffusion, it makes sense to postulate the existence of a reaction front in spherical LiCl particles that defines the boundary between a Li-rich core (blue) and a Na-rich shell (red), as is schematically illustrated in Figure 10. Since the boundary in the salt is established through the limits of random walk diffusion, it should be a diffuse (rather than a sharp) interface involving a concentration gradient. In contrast to the salt phases, it is expected that the ceramic will not have a well-defined boundary between the precursor phase and the product phase as the ion mobility is substantially higher, resulting in a homogeneous distribution (purple) of Li^+ and Na^+ ions in the ceramic.

Experimental evidence for the existence of a concentration gradient can be seen in the peak shapes of powder diffraction data (Figure 11a). At the start of the reaction when single-phase LiCl is present, the salt diffraction peaks are symmetric. As the reaction proceeds, the salt peaks become asymmetric, developing a tail that extends toward the position of the NaCl limit of the LiCl−NaCl solid solution, providing unambiguous evidence for the coexistence of a range of different salt compositions. It is not possible a priori to determine if these peak shapes correspond to inhomogeneity (in the form of a concentration gradient) within each particle or instead to a collection of homogeneous particles with a range of different compositions. However, the observation that under different reaction conditions the same peak shape is observed at the same extent of reaction (Figure 11b) provides strong evidence for concentration gradients.

If we accept the presence of the postulated reaction front, then it is possible to predict how the reaction rate varies with concentration. If the extent of reaction is modest (thin shell approximation), then the extent of the reaction will essentially be linearly proportional to the progress of the reaction front (derivation in Supporting Information). As such, if the Li:Na ratio is increased by a factor of 2, then the amount of material within a given distance from the surface of the salt increases twofold and the reaction rate would also increase twofold. This is very different from the cube root dependence on the Li:Na ratio that is experimentally observed. As such, it suggests that the origin of the cube root behavior is (1) extrinsic to the LiCl salt particles and (2) affects the prefactor (attempt frequency) of the rate-limiting step of diffusion within the salt.

Conventional models for describing the kinetics of solid-state reactions are typically derived by describing the reaction progress in terms of the conversion fraction of the reactants, a quantity denoted by the variable α in a modern review.[29] In

https://doi.org/10.1021/acs.chemmater.2c02543
Chem. Mater. 2023, 35, 917−926

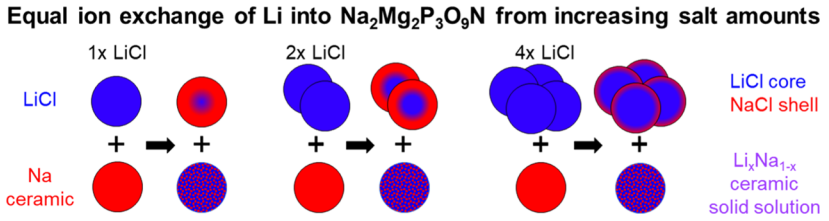

Figure 10. Distribution of Li^+ ions (red) and Na^+ ions (blue) in the salt phase (top row) and ceramic phase (bottom row) before and after partial ion exchange. Since ion mobility in the salt phase is a limiting reaction rate, the salt particles after exchange are expected to have a Na-rich shell and a Li-rich core with a diffuse interface. The thickness of the shell after a fixed number of ions are inserted into the ceramic will be (to a first approximation) inversely proportional to the amount of the salt precursor (Li:Na ratio). In contrast, higher ion mobilities in the ceramic phase should lead to a homogeneous (purple) ion mixture throughout the particles.

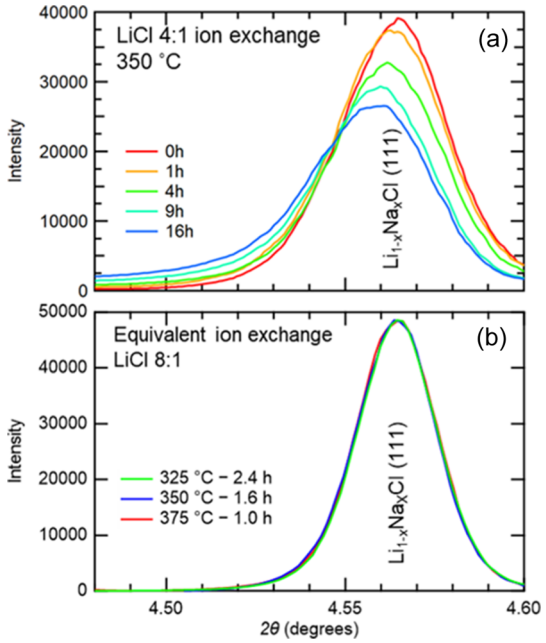

Figure 11. (a) Shape evolution of the (111) salt diffraction peak during ion exchange. (b) Indistinguishable diffraction peak shapes for the equal extent of ion exchange in different reactions (patterns vertically offset for clarity).

this formalism, the $t^{1/2}$ dependence of reaction rate is that which would be expected for the case of 1D diffusion—a very close approximation for the manner in which diffusion-limited solid-state reactions will progress at the surface of a sphere for limited extents of reaction, as was the case for the present studies. However, the cube root scaling that we observe is not tied to the extent of the reaction, α, and as such falls outside of the scope of conventional kinetic models that are agnostic to the rate constant prefactor.

Based on the experimentally observed behavior, we, therefore, hypothesize that cube root dependence is associated with a "radius of capture" around the ceramic $Na_2Mg_2P_3O_9N$ particles. The number of salt particles within a given radius of a ceramic particle will increase as the cube root of the Li:Na ratio, and thus could be the origin of the scaling behavior. The rate of migration of Na^+ ions from the salt to the ceramic will decrease as the Li:Na ratio increases, which will therefore decrease the attempt frequency of the rate-limiting step of the coupled diffusion of Na^+ (entering) and Li^+ (leaving) ions in the salt phase. This postulated mechanism is consistent with the experimentally measured rate behavior observed in the present work and with the E_a associated with the reaction being independent of the Li:Na ratio. However, detailed computational modeling studies of the microscopic transport processes and the gradients that develop in response to them are necessary to validate this (or any alternative) mechanism by demonstrating the ability to quantitatively reproduce the reaction kinetics measured in our in situ synchrotron diffraction studies.

Whether or not the true origin of the concentration scaling behavior derives from a radius of capture, the observed cube root behavior still provides the first general quantitative relationship describing how the rate of solid-state ion exchange depends on the relative quantities of reactants. When combined with the further insights into reaction kinetics provided by the determination of activation energies for hopping and for vacancy formation, it is now possible to make quantitative predictions for how the salt source, the salt vacancy concentration, and the reaction temperature can be optimized to accelerate ion exchange reactions by orders of magnitude.

CONCLUSIONS

High-throughput synchrotron diffraction methods were used to elucidate the factors generally controlling the rate of solid-state reactions. Based on the comparison of synchrotron results with DFT calculations and with prior diffusional studies, it was demonstrated that rate data are consistent with a single thermodynamic activation energy E_a controlling the overall reaction rate, with this E_a always having contributions from a single-ion hopping energy E_{hop} but sometimes also having an additional contribution from a vacancy formation energy, E_{vac}. It was shown that global fitting of rate data for multiple samples can enable the determination of both intrinsic and extrinsic vacancy concentrations, though the careful preparation of a series of samples with consistent surface areas is needed to obtain robust results. Finally, it was discovered that by comparing the rates of reaction using different relative quantities of precursors, the rate-limiting reagent could be clearly identified, and scaling relationships suitable for predicting (and optimizing) the overall reaction rate could be derived.

ASSOCIATED CONTENT

Supporting Information

The Supporting Information is available free of charge at https://pubs.acs.org/doi/10.1021/acs.chemmater.2c02543.

Tab-delimited salt synchrotron collected XRD patterns at room temperature (TXT)

Example TOPAS template input filed used within sequential refinements of ion exchange (TXT)

https://doi.org/10.1021/acs.chemmater.2c02543
Chem. Mater. 2023, 35, 917−926

Representative fits to diffraction data, schematic of experiments, rate data, nominal and actual salt:ceramic molar ratios and doping levels, thin-shell approximation derivation, and calculated shell thicknesses (PDF)

AUTHOR INFORMATION

Corresponding Author

Peter G. Khalifah − *Department of Chemistry, Stony Brook University, New York 11794-3400, United States; Chemistry Division, Brookhaven National Laboratory, New York 11973, United States;* orcid.org/0000-0002-2216-0377; Email: kpete@bnl.gov

Authors

Monty R. Cosby − *Department of Chemistry, Stony Brook University, New York 11794-3400, United States;* orcid.org/0000-0002-2951-7420

Christopher J. Bartel − *Department of Materials Science & Engineering, University of California Berkeley, Berkeley, California 94720, United States; Materials Sciences Division, Lawrence Berkeley National Laboratory, Berkeley, California 94720, United States;* orcid.org/0000-0002-5198-5036

Adam A. Corrao − *Department of Chemistry, Stony Brook University, New York 11794-3400, United States;* orcid.org/0000-0001-6111-8959

Andrey A. Yakovenko − *X-ray Science Division, Advanced Photon Source, Argonne National Laboratory, Lemont, Illinois 60439, United States*

Leighanne C. Gallington − *X-ray Science Division, Advanced Photon Source, Argonne National Laboratory, Lemont, Illinois 60439, United States;* orcid.org/0000-0002-0383-7522

Gerbrand Ceder − *Department of Materials Science & Engineering, University of California Berkeley, Berkeley, California 94720, United States; Materials Sciences Division, Lawrence Berkeley National Laboratory, Berkeley, California 94720, United States;* orcid.org/0000-0001-9275-3605

Complete contact information is available at: https://pubs.acs.org/10.1021/acs.chemmater.2c02543

Author Contributions

P.G.K. and M.R.C. designed the ion exchange experiments. M.R.C. and A.A.C. synthesized samples and did lab XRD validation of their phase purity. The remote experiments were set up by beamline scientists A.A.Y. and L.C.G., enabling M.R.C. to remotely control the data collection. M.R.C. did the synchrotron XRD data analysis under the supervision of P.G.K. DFT calculations were carried out by C.J.B. under the supervision of G.C. The manuscript was primarily written by M.R.C. and P.G.K. with contributions from all co-authors.

Funding

This work was supported as part of GENESIS: A Next Generation Synthesis Center, an Energy Frontier Research Center funded by the U.S. Department of Energy, Office of Science, Basic Energy Sciences under Award Number DE-SC0019212. The work of MRC was in part supported as a part of QuADS: Quantitative Analysis of Dynamic Structures National Science Foundation Research Traineeship Program, Grant Number NSF DGE 1922639.

Notes

The authors declare no competing financial interest.

ACKNOWLEDGMENTS

This research used resources from the Advanced Photon Source, a U.S. Department of Energy (DOE) Office of Science User Facility operated for the DOE Office of Science by Argonne National Laboratory under Contract No. DE-AC02-06CH11357. Data were collected at the 11-ID-B and 17-BM beamlines of the Advanced Photon Source, Argonne National Laboratory. We gratefully acknowledge the exceptional help of beamline scientists Andrey Yakovenko, Leighanne C. Gallington, Tiffany Kinnibrugh, Kevin Beyer, and Olaf Borkiewicz with the remote data collection necessitated by COVID-19 travel restrictions. This research used resources of the National Energy Research Scientific Computing Center (NERSC), a U.S. Department of Energy Office of Science User Facility located at Lawrence Berkeley National Laboratory, operated under Contract No. DE-AC02-05CH11231. This work also used computational resources sponsored by the Department of Energy's Office of Energy Efficiency and Renewable Energy, located at NREL. We thankfully acknowledge interactions with GENESIS team members, especially K. Chapman for the development of and initial training in the use of the multiwell furnace environment, M. McDermott for preliminary discussions on DFT calculations, and J. Neilson for serving as a sounding board during the development of transport models.

REFERENCES

(1) Guo, C. F.; Cao, S.; Zhang, J.; Tang, H.; Guo, S.; Tian, Y.; Liu, Q. Topotactic transformations of superstructures: from thin films to two-dimensional networks to nested two-dimensional networks. *J. Am. Chem. Soc.* **2011**, *133*, 8211−8215.

(2) Lim, J. S.; Lee, J.; Lee, B. J.; Kim, Y.-J.; Park, H.-S.; Suh, J.; Nahm, H.-H.; Kim, S.-W.; Cho, B.-G.; Koo, T. Y.; Choi, E.; Kim, Y.-H.; Yang, C.-H. Harnessing the topotactic transition in oxide heterostructures for fast and high-efficiency electrochromic applications. *Sci. Adv.* **2020**, *6*, No. eabb8553.

(3) Liu, J.; Whitfield, P. S.; Saccomanno, M. R.; Bo, S. H.; Hu, E. Y.; Yu, X. Q.; Bai, J. M.; Grey, C. P.; Yang, X. Q.; Khalifah, P. G. In situ neutron diffraction studies of the ion exchange synthesis mechanism of $Li_2Mg_2P_3O_9N$: evidence for a hidden phase transition. *J. Am. Chem. Soc.* **2017**, *139*, 9192−9202.

(4) Yang, S. P.; Wang, H. Z.; Man, H.; Long, Z. Y.; Yang, J. H.; Sun, S. X.; Ruan, J. F.; Song, Y.; Fang, F. An enhanced Li_3AlH_6 anode prepared by a solid-state ion exchange method for use in a solid-state lithium-ion battery. *Int. J. Electrochem. Sci.* **2020**, *15*, 9487−9498.

(5) Tang, W.; Song, X.; Du, Y.; Peng, C.; Lin, M.; Xi, S.; Tian, B.; Zheng, J.; Wu, Y.; Pan, F.; Loh, K. P. High-performance $NaFePO_4$ formed by aqueous ion-exchange and its mechanism for advanced sodium ion batteries. *J. Mater. Chem. A* **2016**, *4*, 4882−4892.

(6) Clearfield, A. Role of ion-exchange in solid-state chemistry. *Chem. Rev.* **1988**, *88*, 125−148.

(7) Cosby, M. R.; Mattei, G. S.; Wang, Y.; Li, Z.; Bechtold, N.; Chapman, K. W.; Khalifah, P. G. Salt effects on Li-ion exchange kinetics of $Na_2Mg_2P_3O_9N$: systematic in situ synchrotron diffraction studies. *J. Phys. Chem. C* **2020**, *124*, 6522−6527.

(8) Boccardo, G.; Sokolov, I. M.; Paster, A. An improved scheme for a Robin boundary condition in discrete-time random walk algorithms. *J. Comput. Phys.* **2018**, *374*, 1152−1165.

(9) Delay, F.; Ackerer, P.; Danquigny, C. Simulating solute transport in porous or fractured formations using random walk particle tracking: a review. *Vadose Zone J.* **2005**, *4*, 360−379.

(10) Liu, J.; Chang, D. H.; Whitfield, P.; Janssen, Y.; Yu, X. Q.; Zhou, Y. N.; Bai, J. M.; Ko, J.; Nam, K. W.; Wu, L. J.; Zhu, Y. M.; Feygenson, M.; Amatucci, G.; Van der Ven, A.; Yang, X. Q.; Khalifah, P. Ionic conduction in cubic $Na_3TiP_3O_9N$, a secondary Na-ion battery cathode with extremely low volume change. *Chem. Mater.* **2014**, *26*, 3295−3305.

(11) Ashiotis, G.; Deschildre, A.; Nawaz, Z.; Wright, J. P.; Karkoulis, D.; Picca, F. E.; Kieffer, J. The fast azimuthal integration Python library: pyFAI. *J. Appl. Crystallogr.* **2015**, *48*, 510−519.
(12) Coelho, A. A. TOPAS and TOPAS-Academic: an optimization program integrating computer algebra and crystallographic objects written in C++. *J. Appl. Crystallogr.* **2018**, *51*, 210−218.
(13) Kresse, G.; Furthmüller, J. Efficient iterative schemes for ab initio total-energy calculations using a plane-wave basis set. *Phys. Rev. B: Condens. Matter Mater. Phys.* **1996**, *54*, 11169−11186.
(14) Perdew, J. P.; Burke, K.; Ernzerhof, M. Generalized gradient approximation made simple. *Phys. Rev. Lett.* **1996**, *77*, 3865−3868.
(15) Kresse, G.; Joubert, D. From ultrasoft pseudopotentials to the projector augmented-wave method. *Phys. Rev. B: Condens. Matter Mater. Phys.* **1999**, *59*, 1758−1775.
(16) Jain, A.; Ong, S. P.; Hautier, G.; Chen, W.; Richards, W. D.; Dacek, S.; Cholia, S.; Gunter, D.; Skinner, D.; Ceder, G.; Persson, K. A. Commentary: The Materials Project: a materials genome approach to accelerating materials innovation. *APL Mater.* **2013**, *1*, 011002.
(17) Monkhorst, H. J.; Pack, J. D. Special points for Brillouin-zone integrations. *Phys. Rev. B: Solid State* **1976**, *13*, 5188−5192.
(18) Ong, S. P.; Richards, W. D.; Jain, A.; Hautier, G.; Kocher, M.; Cholia, S.; Gunter, D.; Chevrier, V. L.; Persson, K. A.; Ceder, G. Python Materials Genomics (pymatgen): A robust, open-source python library for materials analysis. *Comput. Mater. Sci.* **2013**, *68*, 314−319.
(19) Henkelman, G.; Uberuaga, B. P.; Jónsson, H. A climbing image nudged elastic band method for finding saddle points and minimum energy paths. *Chem. Phys.* **2000**, *113*, 9901−9904.
(20) Cros, C.; Hanebali, L.; Latie, L.; Villeneuve, W.; Gang, W. Structure, ionic motion and conductivity in some solid-solutions of the $LiClMCl_2$ systems (M= Mg, V, Mn). *Solid State Ion.* **1983**, *9*−*10*, 139−147.
(21) Okadome Valencia, H.; Wang, B.; Frapper, G.; Rohl, A. L. New developments in the GDIS simulation package: Integration of VASP and USPEX. *J. Comput. Chem.* **2021**, *42*, 1602−1626.
(22) He, B.; Chi, S.; Ye, A.; Mi, P.; Zhang, L.; Pu, B.; Zou, Z.; Ran, Y.; Zhao, Q.; Wang, D.; Zhang, W.; Zhao, J.; Adams, S.; Avdeev, M.; Shi, S. High-throughput screening platform for solid electrolytes combining hierarchical ion-transport prediction algorithms. *Sci. Data* **2020**, *7*, 151.
(23) Haven, Y. The ionic conductivity of Li-halide crystals. *Recl. Trav. Chim. Pays-Bas* **1950**, *69*, 1471−1489.
(24) Catlow, C.; Corish, J.; Diller, K.; Jacobs, P.; Norgett, M. The contribution of vacancy defects to mass transport in alkali halides-an assessment using theoretical calculations of defect energies. *J. Phys. C: Solid State Phys.* **1979**, *12*, 451.
(25) Shimoji, M.; Hoshino, H. Thermoelectric power of ionic crystals—I general theory. *J. Phys. Chem. Solids* **1967**, *28*, 1155−1167.
(26) Laredo, E. A. d.; Dartyge, E. Ionic conductivity of NaCl: $SrCl_2$ crystals. *J. Chem. Phys.* **1970**, *53*, 2214−2222.
(27) Goodenough, J. B.; Hong, H. Y. P.; Kafalas, J. A. Fast Na^+-ion transport in skeleton structures. *Mater. Res. Bull.* **1976**, *11*, 203−220.
(28) Yoon, D. N.; Lazarus, D. Pressure dependence of ionic conductivity in KCl, NaCl, KBr, and NaBr. *Phys. Rev. B: Solid State* **1972**, *5*, 4935−4945.
(29) Khawam, A.; Flanagan, D. R. Solid-state kinetic models: basics and mathematical fundamentals. *J. Phys. Chem. B* **2006**, *110*, 17315−17328.

https://doi.org/10.1021/acs.chemmater.2c02543
Chem. Mater. 2023, 35, 917−926